



## Full length article

## Anelasticity induced by AC flash processing of cubic zirconia



Hiroshi Masuda<sup>a,\*</sup>, Koji Morita<sup>b</sup>, Tomoharu Tokunaga<sup>c</sup>, Takahisa Yamamoto<sup>c</sup>,  
Hidehiro Yoshida<sup>a,d</sup>

<sup>a</sup> Department of Materials Science and Engineering, School of Engineering, The University of Tokyo, 7-3-1 Hongo, Bunkyo-ku, Tokyo 113-8656, Japan

<sup>b</sup> Research Center for Functional Materials, National Institute for Materials Science, 1-2-1 Senzen, Ibaraki, Tsukuba 305-0047, Japan

<sup>c</sup> Department of Materials Design Innovation Engineering, School of Engineering, Nagoya University, Furo-cho, Chikusa-ku, Nagoya 464-8603, Japan

<sup>d</sup> Next generation Zirconia Social Cooperation Program, Institute of Engineering Innovation, The University of Tokyo, 7-3-1 Hongo, Bunkyo-ku, Tokyo 113-8656, Japan

## ARTICLE INFO

## Article history:

Received 5 August 2021

Revised 31 January 2022

Accepted 31 January 2022

Available online 4 February 2022

## Keywords:

Ceramics

Flash sintering

Viscoelasticity

Pseudoelasticity

Nanoindentation

## ABSTRACT

The defect physics is important for understanding the athermal effect of electric fields and/or currents on the enhanced ionic diffusion during flash sintering of ceramics. In this study, conventionally sintered 8 mol% yttria-stabilized zirconia with a fluorite cubic structure was processed by AC flash and subsequently quenched to partially freeze the flash-induced defect structures. The dynamic and quasi-static mechanical properties of flashed and non-flashed samples were evaluated by a sound velocity measurement and a nanoindentation technique to characterize the mechanical responses attributed to the flash-induced defects. A negligible change was confirmed in the dynamic elastic constants even after flash, while the quasi-static elastic properties of the flashed sample exhibited a considerable rate dependence (i.e., the slower the loading rate, the lower the measured contact modulus). The contact modulus of the flashed sample tested at the slowest loading rate in this study was reduced to approximately 72% of the non-flashed one, where the contact modulus was rate-independent. The time-dependent mechanical behavior was also confirmed during nanoindentation creep. Such rate- and time-dependent mechanical properties are characterized as anelasticity (i.e., viscoelasticity or pseudoelasticity in other terms), which can be attributed to stress-induced and thermally activated recoverable motions of point defects. The flash process of cubic zirconia possibly induced point defects associated with short-range structural change, which could be the origin of anelasticity.

© 2022 The Author(s). Published by Elsevier Ltd on behalf of Acta Materialia Inc.  
This is an open access article under the CC BY license (<http://creativecommons.org/licenses/by/4.0/>)

## 1. Introduction

Flash sintering, in which ceramics green compact is densified in a few seconds by applying an electric field beyond threshold strength at a specific furnace temperature, has been extensively studied since it was firstly reported in 2010 [1]. Applications of flash sintering in various oxide ceramics have been demonstrated over the past decade [2–8]. Furthermore, flash events have also been reported in bulk single crystals and polycrystals [9–13]. In particular, polycrystalline ceramics under a flash state exhibit high-strain-rate superplasticity and enhanced crack healing at low furnace temperatures [11–13]. Flash events kinetically accelerate high-temperature dynamics such as sintering, superplasticity, and crack healing, implying that ionic diffusion in ceramics is enhanced by

flash. Such an enhanced diffusion can be attributed to thermal and athermal effects of electric fields and/or currents:

- (1) Thermal effect – flash events are triggered by thermal runaway through Joule heating and positively temperature-dependent electric conductivity [14]. Hence, a sample temperature substantially increases by flash, resulting in enhanced diffusion even at low furnace temperatures. Many literature reported that microstructural evolutions such as densification and/or grain growth during flash sintering are correlated with sample temperatures [15–18].
- (2) Athermal effect – despite the temperature rise caused by Joule heating, kinetic analysis indicates that the rates of flash sintering and superplasticity should still be orders of magnitude higher than conventional ones [12,19]. This suggests that electric fields and/or currents have athermal effects on ionic diffusion of ceramics in addition to the thermal aspect. It is noteworthy that such athermal effects were suggested

\* Corresponding author.

E-mail address: [masuda@material.t.u-tokyo.ac.jp](mailto:masuda@material.t.u-tokyo.ac.jp) (H. Masuda).

not only in the powder densification process but in the bulk deformation [12].

Recently, the mechanism of this athermal effect on ionic diffusion during flash is attracting extensive interest among researchers [20–22]. A contribution of Frenkel defects potentially induced by flash was early suggested by Raj et al. [23], which has been supported by several experimental [24–27] and numerical studies [28–30]. In contrast, a few reports have disagreed with such formations of Frenkel defects during flash [31,32]. Several studies have highlighted the importance of electrochemical reduction sometimes accompanied by sample blackening, suggesting the importance of oxygen deficiency during flash [33–35]. *In-situ* X-ray diffraction (XRD) studies using synchrotron radiations reported phase transitions [36,37] and/or anisotropic lattice expansions during flash [24,25]. Anomalous electrical [17], optical [9,38–40], and mechanical properties [27,41–43] of flash-sintered ceramics have also been demonstrated. The literature suggests different opinions on this topic, while they are all looking for point defects responsible for the athermal effect, their local structure, and kinetic roles in flash. These inconsistencies can be due to several problems:

- (1) Electrochemical reactions in DC flash – most of the past studies on flash sintering have adopted DC methods. Here, long-range electromigration of ions and resultant chemical reactions, like cathodic reduction, have often been observed [10,33–35]. However, defects derived from these electrochemical reactions polarized near the electrodes and their effects on diffusional kinetics should be distinguished from the athermal ones, possibly excluded by an AC electric field where such polarized defect accumulation is restricted [10,18]. Even in AC flash sintering, abrupt densification and grain growth comparable to those in DC flash [18] and the enhancement of photoluminescence [39,40] were reported to date. Hence, the flash-induced defect nature, except for the electrochemical ones, can also be evaluated using the AC method.
- (2) Recovery of defects – post-mortem analysis of flash-sintered samples can miss the defects which have thermally recovered before the samples are cooled down. *In-situ* experiments are powerful solutions against this problem [24,25,27,34,36,37], while they are cost-consuming and have considerable limitations in sample characterization. It can also be effective to quench the defect structures under a flash state by adopting low furnace temperatures and high current densities. Such frozen samples can be characterized by *ex-situ* but more flexible methods.

In this study, 8 mol% yttria-stabilized zirconia (8YSZ) with a fluorite cubic structure, which was fully sintered and sufficiently annealed before flash processing, was used as the starting material to minimize the potential effects of microstructural evolutions such as densification and grain growth during flash sintering. AC flash processing was used to suppress the long-range electromigration of ions. The structure under flash was partially frozen by a quench method with its maximum cooling rate exceeding  $300^{\circ}\text{C}\cdot\text{s}^{-1}$ . The furnace temperature was set as low as  $600^{\circ}\text{C}$  which is near the lower bound for oxygen ionic diffusion in YSZ. The dynamic and quasi-static mechanical properties, crystal structures, and microstructures of the flashed and quenched samples were characterized using *ex-situ* methods to detect a signal from the flash-induced defects. A particular focus was placed on the elastic properties of the flashed sample, as motivated by the recently reported concept of flash-induced elastic softening [27].

Several important phenomena associated with flash sintering, such as current localization at interparticle necking during the densification step [20], might be excluded in this study using the

fully densified sample. However, defect characterization related to flash should be possible even with the densified material as the enhanced diffusion occurs not only in the powder densification process but in the bulk phenomena such as superplasticity of YSZ [11,12].

## 2. Methods

### 2.1. Materials and processing

Commercial powders of 8YSZ (TZ-8Y, Tosoh, Japan) were compacted via hand pressing at 0.6 MPa and subsequent cold isostatic pressing at 392 MPa for 10 min. The powder green compact was fully densified through conventional sintering at  $1250^{\circ}\text{C}$  for 40 h, then machined into a rectangular rod shape of  $1.8 \times 2.5 \times 23 \text{ mm}^3$ , and annealed at  $1700^{\circ}\text{C}$  for 5 h for sufficient grain growth [44].

Platinum electrodes were coated on the sample ends with an electrode distance of 10 mm (JEC-3000FC, JEOL, Japan). The sample was suspended via platinum wires connected to an AC power supply (POP200-1.75, Matsusada Precision, Japan) and heated up to  $600^{\circ}\text{C}$  in an atmospheric furnace. A square-wave AC electric field with a frequency of 100 Hz and a field strength amplitude of  $220 \text{ V}\cdot\text{cm}^{-1}$  was applied to the sample for inducing a flash event. The power supply was switched from the voltage- to current-control modes when the current density increased up to  $40 \text{ mA}\cdot\text{mm}^{-2}$ . Subsequently, the current amplitude was increased by  $20 \text{ mA}\cdot\text{mm}^{-2}\cdot\text{s}^{-1}$  up to  $400 \text{ mA}\cdot\text{mm}^{-2}$ , where the sample was quenched by turning off the power supply after a holding time of 600 s. The surface temperature during flash and quench was measured using a unicolor pyrometer (IR-CAS, Chino, Japan).

### 2.2. Dynamic mechanical characterization

Dynamic Young's modulus ( $E$ ) and Poisson's ratio ( $\nu$ ) were evaluated through a sound velocity measurement (5073PR, Olympus, Japan). The  $E$  and  $\nu$  values were calculated from the measured longitudinal and transversal sound velocities ( $V_L$  and  $V_T$ ) using the following equations [45]:

$$E = \rho V_T^2 \frac{3V_L^2 - 4V_T^2}{V_L^2 - V_T^2} \quad (1)$$

and

$$\nu = \frac{V_L^2 - 2V_T^2}{2(V_L^2 - V_T^2)}, \quad (2)$$

where  $\rho$  is the measured sample density,  $5.957 \text{ g}\cdot\text{cm}^{-3}$ .

### 2.3. Quasi-static micromechanical characterization

Quasi-static micromechanical properties, such as contact modulus ( $E^*$ ), hardness ( $H$ ), and creep behaviors, were characterized using a nanoindentation facility (TI980, Bruker Nano Surface Division, USA). The sample polishing was finished by  $0.125 \mu\text{m}$  diamond slurry. Beforehand, the flashed samples were ground to a thickness of 0.9 mm to measure the micromechanical properties at the sample cross sections. The nanoindentation experiments were performed at ambient conditions using a Berkovich diamond tip. The  $E^*$  and  $H$  values were calculated from the measured load-displacement ( $P-h$ ) relations via the standard Oliver-Pharr method [46] using fused quartz for preliminary calibration ( $E^* = 69.6 \text{ GPa}$ ).

The spatial distributions of  $E^*$  and  $H$  in the flashed sample were mapped in an area of  $2.0 \times 5.0 \text{ mm}^2$  by 0.2 mm pitches at a constant loading rate (= unloading rate) of  $1 \times 10^0 \text{ mN}\cdot\text{s}^{-1}$  up to the maximum force of 5 mN. Rate-controlled experiments were

also performed at different loading rates (= unloading rate) from  $1 \times 10^{-1}$  to  $1 \times 10^2 \text{ mN}\cdot\text{s}^{-1}$  up to the maximum force of 5 mN. These experiments were carefully conducted within a specific area where the spatial distributions of  $E^*$  and  $H$  were relatively uniform (i.e., each standard deviation is less than 10% of the local average in the above experiment). The  $E^*$  values were compared with the theoretical contact moduli,  $E_{\text{th}}^*$ , estimated from the measured dynamic elastic parameters,  $E$  and  $\nu$ , using the following equation [46]:

$$E_{\text{th}}^* = \left( \frac{1 - \nu^2}{E} + \frac{1 - \nu_{\text{tip}}^2}{E_{\text{tip}}} \right)^{-1} \quad (3)$$

where  $E_{\text{tip}}$  and  $\nu_{\text{tip}}$  are Young's modulus (1140 GPa) and Poisson's ratio (0.07) of diamond [47].

Furthermore, nanoindentation creep experiments were conducted with a holding time of 200 s at the constant load of 5 mN, up to which the loading rate was set as high as  $1 \times 10^1 \text{ mN}\cdot\text{s}^{-1}$  to suppress the creep strain during the loading sequence. The effective creep strain rate,  $\dot{\varepsilon}_{\text{eff}}$ , was estimated from the equation below:

$$\dot{\varepsilon}_{\text{eff}} = \frac{1}{h} \left( \frac{dh}{dt} \right) \quad (4)$$

where  $h$  is the displacement and  $t$  is time [48].

#### 2.4. Crystal structure and microstructural characterization

The crystal structures were evaluated by XRD measurements using Cu  $\text{K}\alpha 1$  and  $\text{K}\alpha 2$  radiations (Smart Lab., Rigaku, Japan). The sample surfaces were polished as described in Section 2.3 and thermally etched at  $1100^\circ\text{C}$  for 0.5 h. The XRD profiles were obtained in the angular range of  $2\theta = 20^\circ\text{--}80^\circ$ .

The microstructures were characterized via transmission electron microscopy (TEM; JEM-2100Plus, JEOL, Japan) and electron backscatter diffraction (EBSD) in a scanning electron microscope facility (JSM-7000F, JEOL, Japan). The TEM foils were prepared by mechanical thinning and argon ion milling. For the EBSD observation, the sample surfaces were thermally etched at  $1300^\circ\text{C}$  for 0.5 h and coated by amorphous osmium with a thickness of approximately 1 nm via plasma chemical vapor deposition (NEOC-ST, Meiwafosis, Japan). The standard crystal information of 8YSZ ( $Fm3m$ ;  $a = 0.5132 \text{ nm}$  [49]) was used as the reference structure. The average grain size ( $d_{\text{avg}}$ ) was estimated from the EBSD measurement using the equation below [50]:

$$d_{\text{avg}} = \frac{\pi}{2} d_{\text{int}} \quad (5)$$

where  $d_{\text{int}}$  is the average intercept length at grain boundaries calculated from the EBSD analysis software (OIM Analysis Station, TSL EDAX, USA).

## 3. Results

### 3.1. Thermoelectric responses during flash

Fig. 1 shows representative sample appearance and thermoelectric responses during flash. This process was visually homogeneous, with uniform thermal radiation emitted throughout the sample between electrodes (Fig. 1a). After the electric field was applied, the flash event occurred with a short incubation time of a few seconds (Fig. 1b). Then, the current density was increased with a decrease in the field strength and eventually held at  $400 \text{ mA}\cdot\text{mm}^{-2}$  for 600 s. Except for several voltage surges, the

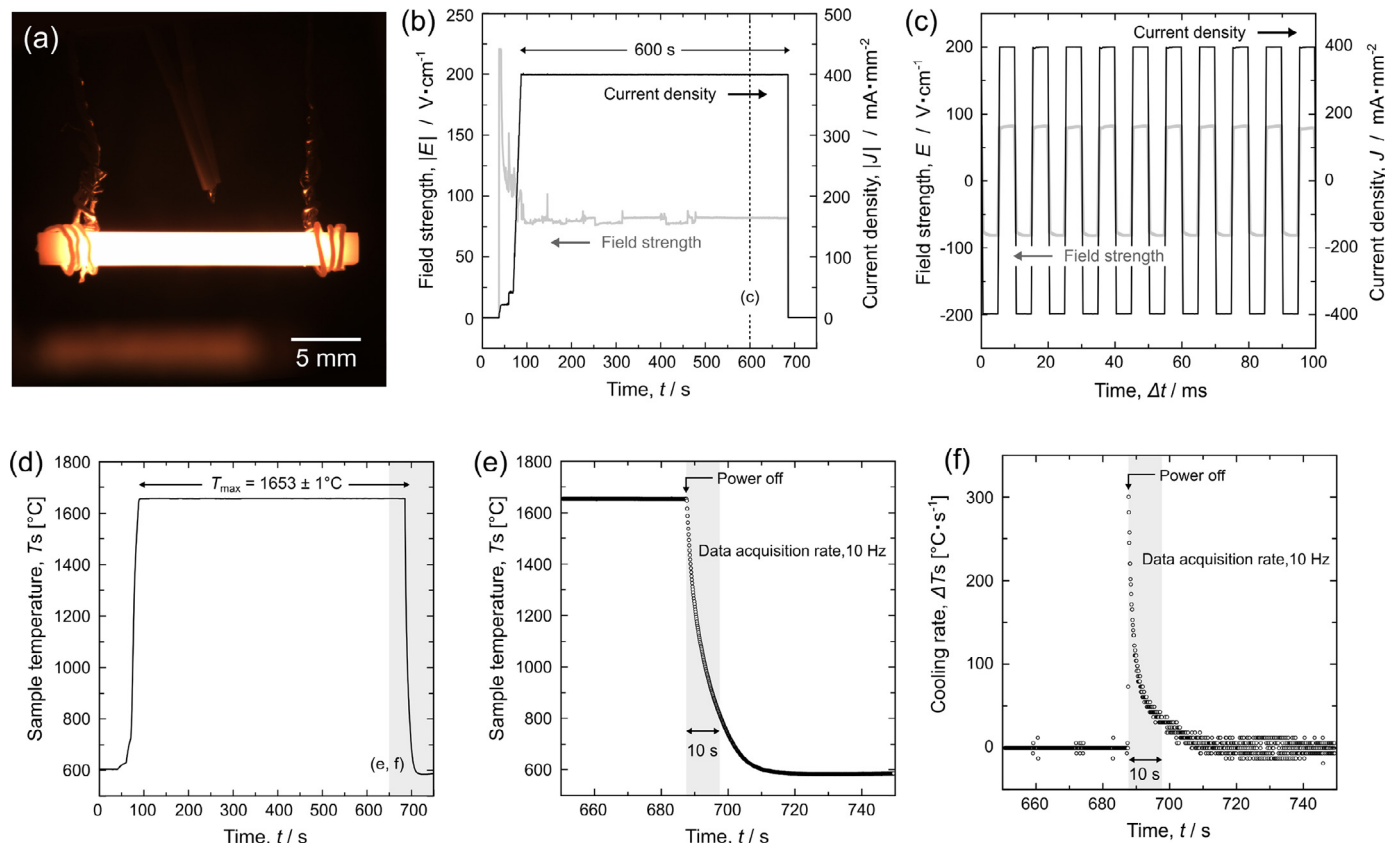


**Fig. 1.** (a) Representative sample image in flash processing, (b) time histories of the field strength (gray; left axis) and current density (black; right axis) amplitudes, (c) the field strength (gray; left axis) and current density (black; right axis) in a short time span around  $t = 600 \text{ s}$ , (d) the time history of the sample temperature measured using a pyrometer, (e) the sample temperature and (f) the cooling rate before and during the quench process.

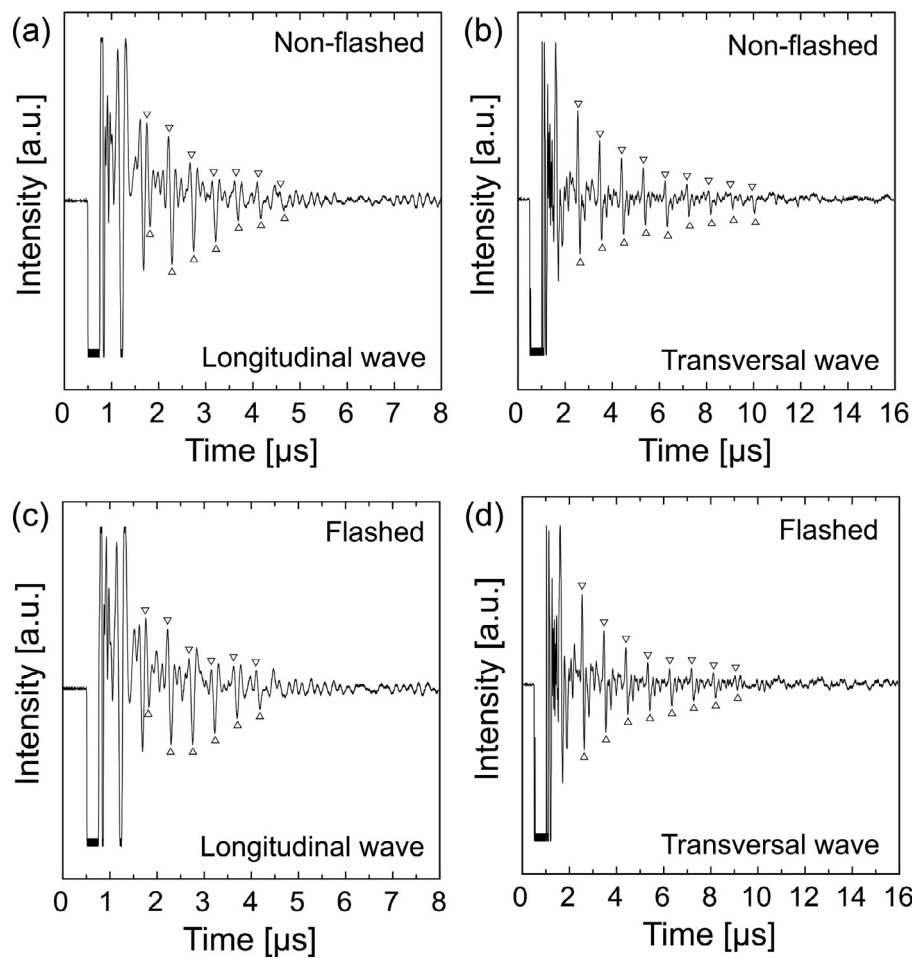


**Fig. 2.** Representative longitudinal (left column) and transversal (right column) sound echo traces obtained from sound velocity measurements for (a) (b) non-flashed and (c) (d) flashed samples.

**Table 1**

Longitudinal and transversal sound velocities,  $V_L$  and  $V_T$ , respectively, and the corresponding dynamic Young's modulus,  $E$ , and Poisson's ratio,  $\nu$ .

Number, $n$	Longitudinal velocity, $V_L$ [km·s <sup>-1</sup> ]	Transversal velocity, $V_T$ [km·s <sup>-1</sup> ]	Dynamic Young's modulus, $E$ [GPa]	Poisson's ratio, $\nu$
Non-flashed	6	7.54 ± 0.12	3.82 ± 0.03	231 ± 4
Flashed	6	7.53 ± 0.12	3.80 ± 0.05	229 ± 6

field and current responses were stably controlled with no phase shift (Fig. 1c). With the increase in current density, the sample temperature also increased and eventually settled at 1653°C ± 1°C (Fig. 1d). As the power supply was turned off, the sample temperature rapidly decreased to the furnace temperature; the sample was cooled down to approximately 800°C in the initial 10 s (Fig. 1e). The maximum cooling rate exceeded 300°C·s<sup>-1</sup> within the time resolution of this experiment (Fig. 1f). Sample blackening after flash was not recognized in this study.

### 3.2. Dynamic elastic properties

Fig. 2 shows representative longitudinal and transversal sound echo traces, demonstrating the periodic pulse-like waveforms. The sound echoes were considerably reproducible among all the measurements since the fully densified samples were used in this study. The sound velocity was measured from the peak intervals of each waveform and sample thickness. Table 1 summarizes the average sound velocities ( $V_L$  and  $V_T$ ) and corresponding dynamic elastic constants ( $E$  and  $\nu$ ) of each sample. Negligible differences in

the sound velocities and the elastic constants were confirmed between the flashed and non-flashed samples. Thus, the elastic softening (i.e., change in the elastic constants) after flash, which was expected from the previous report [27], was not recognized in this experiment. As discussed later, the literature might catch anelastic effects that can cause an apparent decrease in quasi-static elastic moduli.

### 3.3. Quasi-static micromechanical properties

#### 3.3.1. Spatial distribution

Fig. 3 shows representative  $E^*$  and  $H$  distributions on the cross section after flash, obtained via nanoindentation mapping at a constant loading rate of  $1 \times 10^0$  mN·s<sup>-1</sup>. The  $E^*$  and  $H$  values at this loading rate were ranged in approximately 135–190 GPa and 14.0–17.0 GPa, respectively. This spatial distribution is possibly attributed to the intensity gradients of local field strengths, current densities, temperatures, and their time histories during the flash processing. In contrast, the non-flashed sample showed uniform contact modulus and hardness values,  $E^* = 221 \pm 5$  GPa and

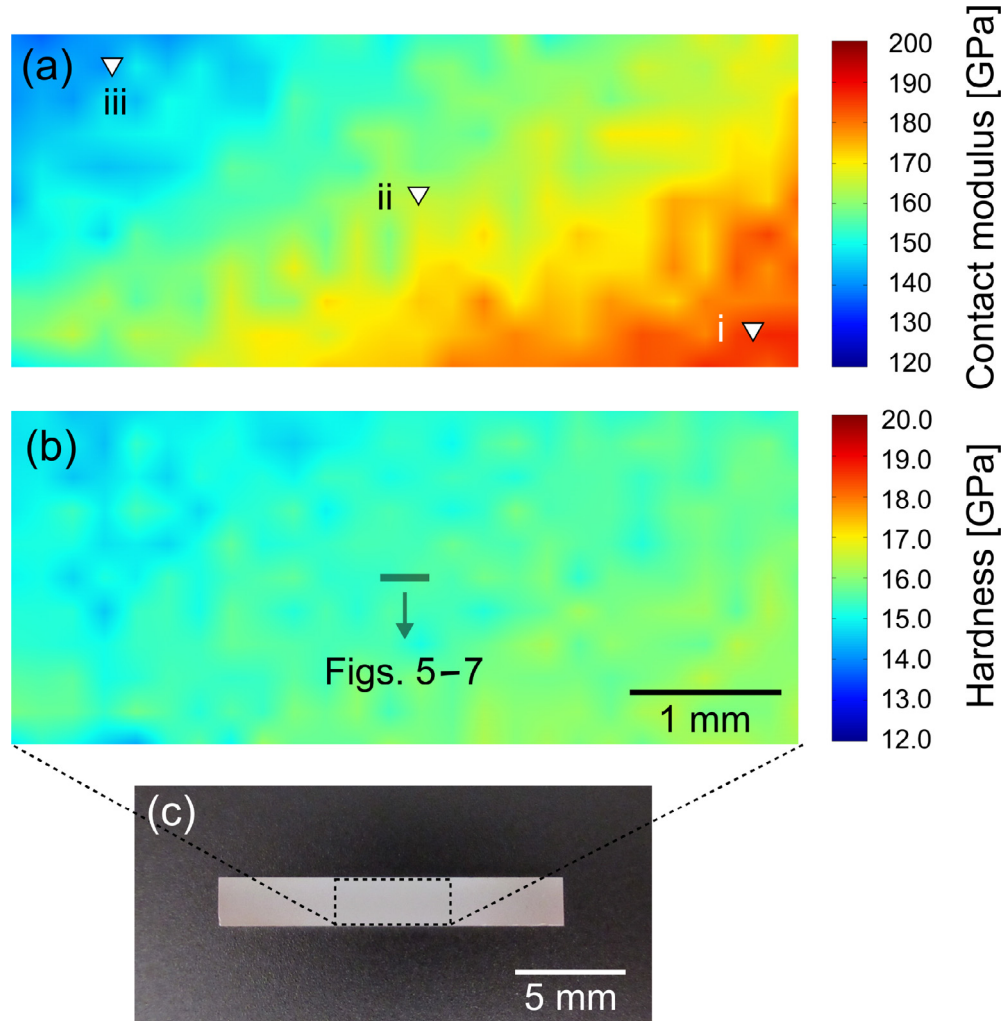


**Fig. 3.** Spatial distributions of (a) contact modulus,  $E^*$ , and (b) hardness,  $H$ , in the flashed sample measured by nanoindentation experiments at a constant loading rate (= unloading rate) of  $1 \times 10^0$  mN·s $^{-1}$  up to the maximum force of 5 mN with 0.2 mm pitches. The nanoindentation measurements were performed on the sample cross section shown in (c). The applied field direction was horizontal.

$H = 17.2 \pm 0.3$  GPa, at this loading rate, which are close to those reported for this material in the literature [51–55].

Fig. 4 demonstrates representative  $P$ - $h$  relations and corresponding impression images. Despite the considerable variety in the  $H$  values calculated from the  $P$ - $h$  relations, the impression sizes appear almost constant, ca.  $0.70 \pm 0.02$   $\mu\text{m}$ . This suggests that true hardness (i.e., the intrinsic resistance to plastic deformation) was not reduced by flash processing but underestimated due to the substantial reduction in the contact modulus of the flashed sample.

### 3.3.2. Rate dependence

Fig. 5 shows the  $E^*$  and  $H$  values of flashed and non-flashed samples as functions of loading rates ranging from  $1 \times 10^{-1}$  to  $1 \times 10^2$  mN·s $^{-1}$ . The data after flash were obtained within the rectangular area shown in Fig. 3b to minimize the effect of spatial distributions. Here, the actual biases due to the spatial distribution were approximately 5% and 2% of the local averages for the  $E^*$  and  $H$  measurements, respectively.

The  $E^*$  values of the flashed sample were positively dependent on the loading rate, while the non-flashed one exhibited negligible rate dependence and are comparable to the theoretical contact modulus  $E_{\text{th}}^*$ , derived from the sound velocity measurement (gray range in Fig. 5a). Hence, the non-flashed sample was almost elasto-

plastic, while the flashed one exhibited rate-dependent and recoverable anelastic deformation under quasi-static conditions.

In contrast, both flashed and non-flashed samples showed the rate dependence of  $H$ . The slopes of  $H$  values against loading rates were almost equivalent for the flashed and non-flashed data but with a rate-independent gap of 1.8 GPa. Fig. 6 demonstrates representative  $P$ - $h$  relations at different loading rates and corresponding impression images. The impression sizes decreased with the increasing loading rate, which was unnecessarily consistent with the  $H$  values calculated from the  $P$ - $h$  curves. Hence, the true hardness was dominated by the rate-dependent plasticity (i.e., dislocation activities) and was negligibly affected by the flash processing and associated defect nucleation. The underestimation of  $H$  in the flashed sample was caused by the recoverable anelastic strain and reduction in the contact modulus. This is also supported by micro-Vickers indentation experiments, where the hardness measured from the impression sizes was negligibly changed after the flash processing (Supplementary Fig. S1 and Table S1).

A similar rate dependence and reduction in the  $E^*$  and  $H$  values were also confirmed in 3 mol% yttria-stabilized zirconia (3YSZ) after an AC flash processing (Supplementary Figs. S2 and S3). Hence, such anelastic responses can be widely obtained among the zirconia–yttria solid solutions using flash processing.

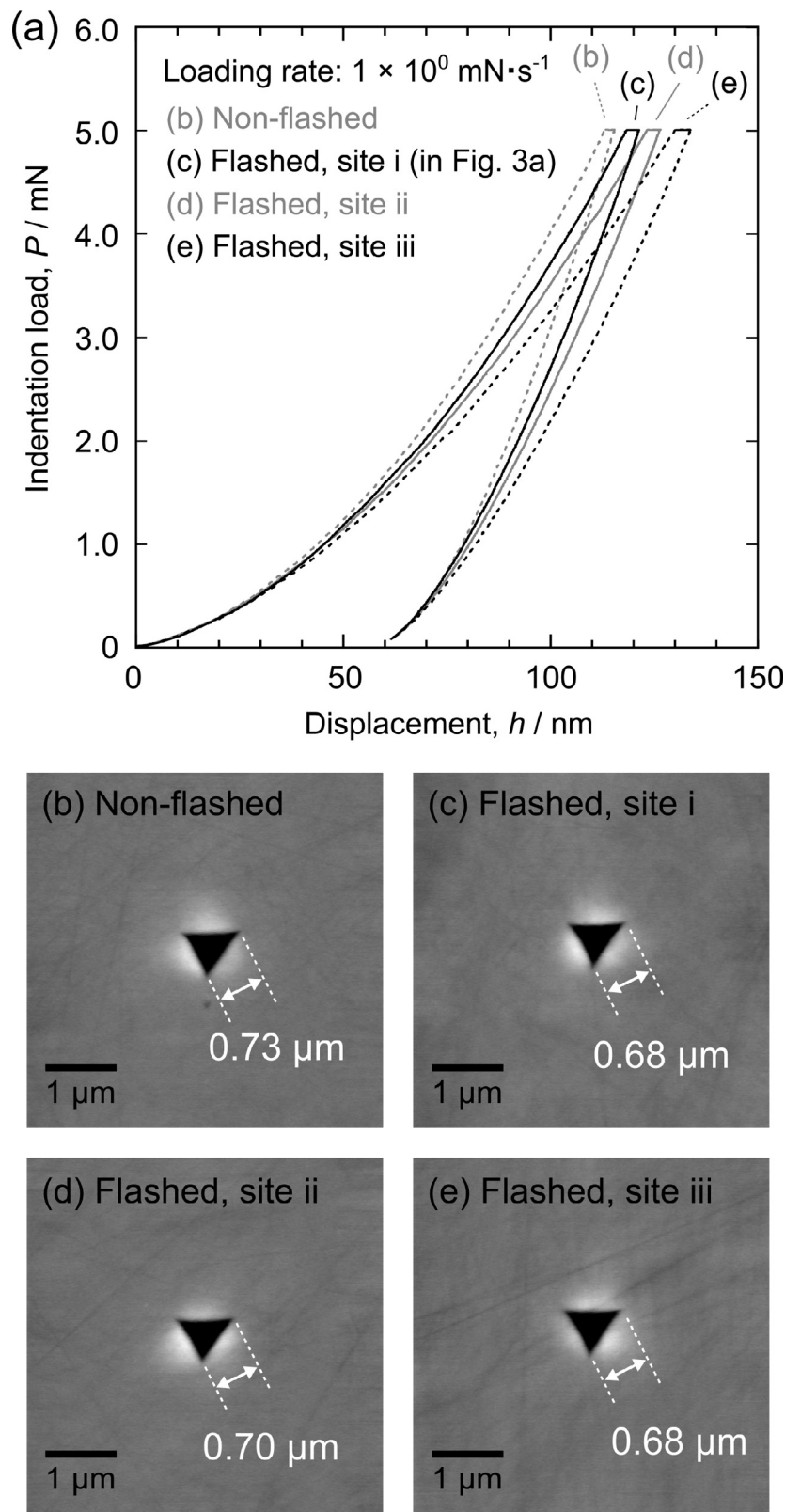


**Fig. 4.** (a) Representative  $P$ - $h$  curves during nanoindentation experiments at a constant loading rate of  $1 \times 10^0 \text{ mN}\cdot\text{s}^{-1}$  and corresponding impression SPM images obtained from (b) the non-flashed sample, (c) site i, (d) site ii, and (e) site iii in the flashed one. These site positions are indicated in Fig. 3(a) by white triangles.

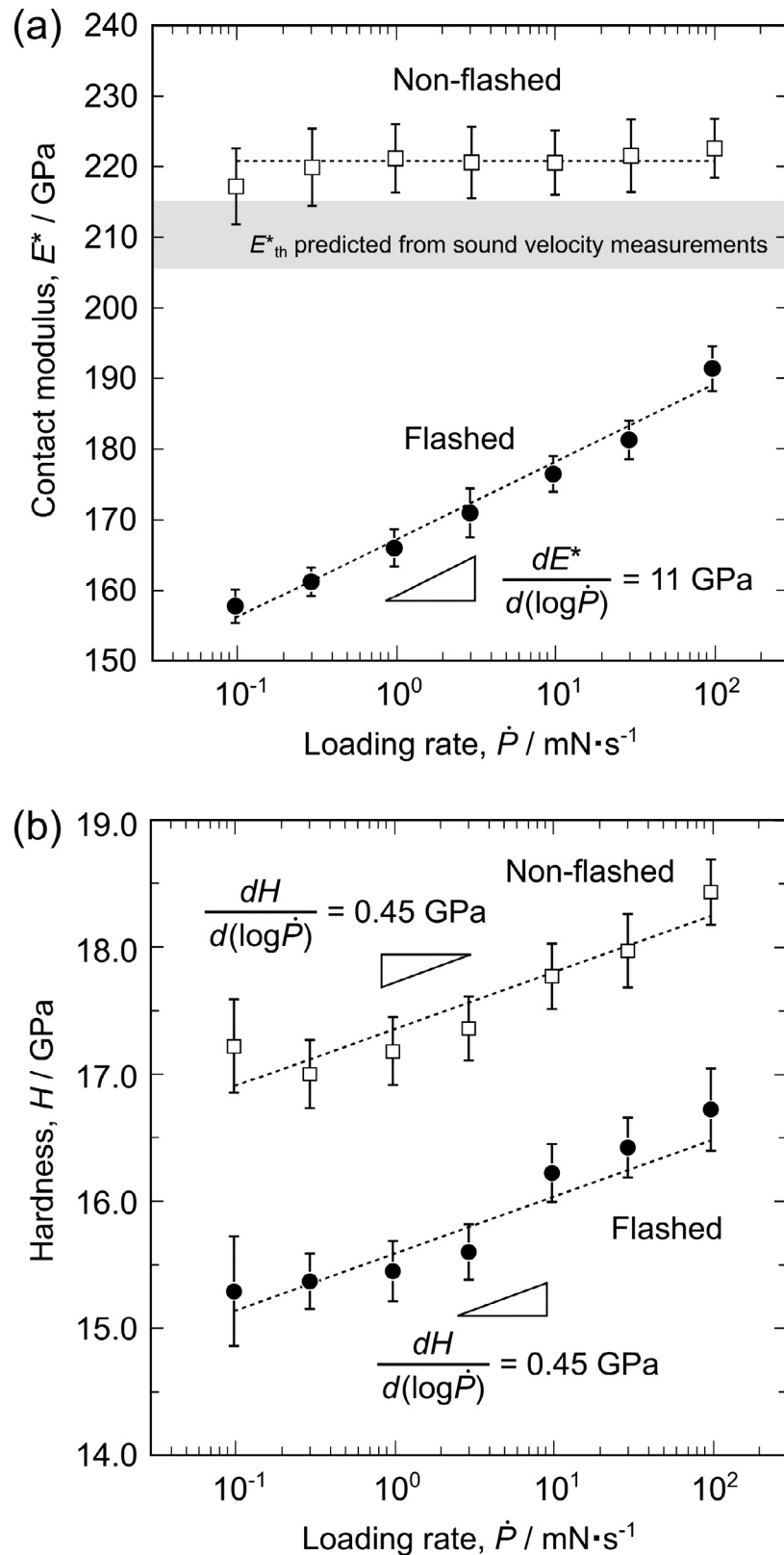


**Fig. 5.** (a) Contact modulus,  $E^*$ , and (b) hardness,  $H$ , as functions of loading rates measured by nanoindentation experiments of non-flashed (white squares) and flashed (black circles) samples. The data were obtained within the area indicated by the gray rectangle in Fig. 3(b). The gray band in (a) indicates the  $E^*$  range predicted from the sound velocity measurement.

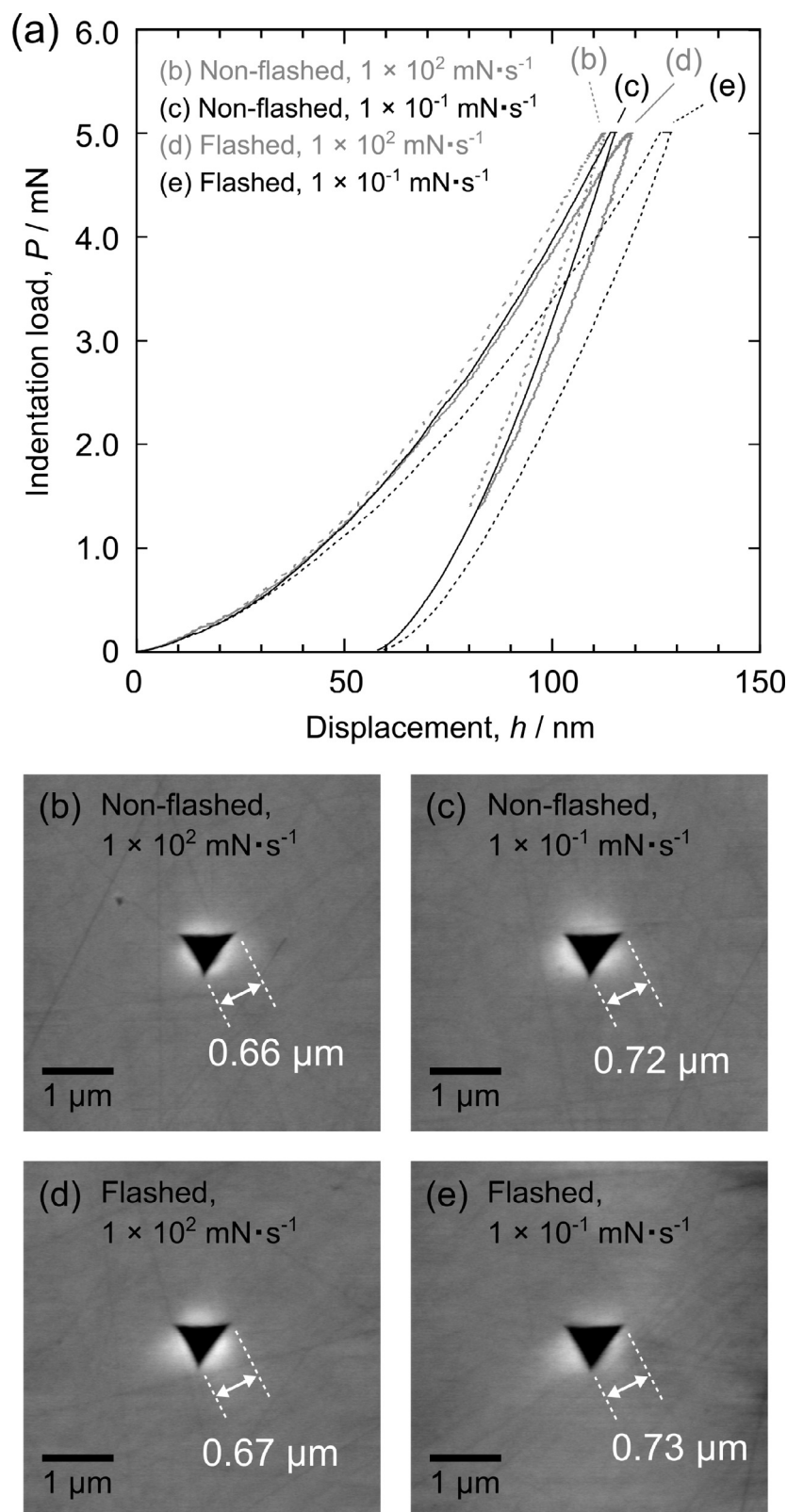


**Fig. 6.** (a) Representative  $P$ - $h$  curves during nanoindentation experiments at different loading rates of  $1 \times 10^2 \text{ mN}\cdot\text{s}^{-1}$  (gray) and  $1 \times 10^{-1} \text{ mN}\cdot\text{s}^{-1}$  (black) and corresponding impression SPM images obtained from (b) (c) the non-flashed and (d) (e) flashed samples.

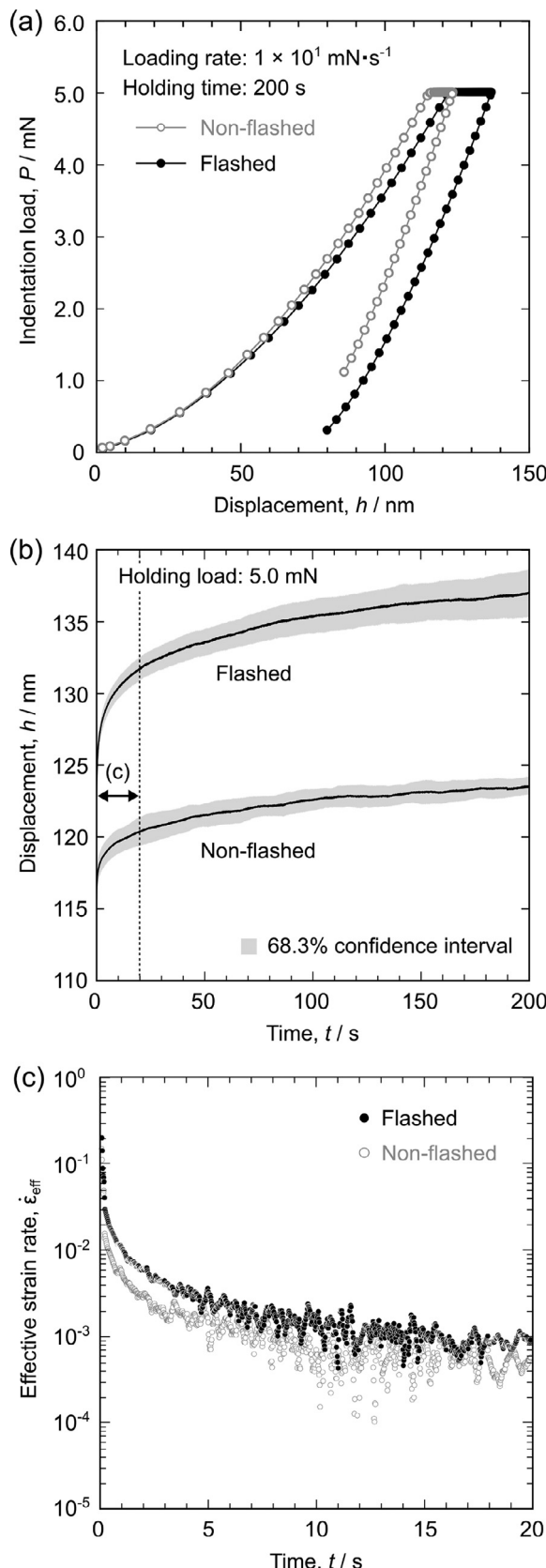


**Fig. 7.** (a) Representative  $P$ - $h$  curves during nanoindentation creep of non-flashed (gray) and flashed (black) samples at 5 mN for 200 s, (b) the average creep curves during the holding sequences, merged with  $n > 5$  data, and (c) the average effective strain rate as functions of time in the initial 20 s.

### 3.3.3. Time dependence

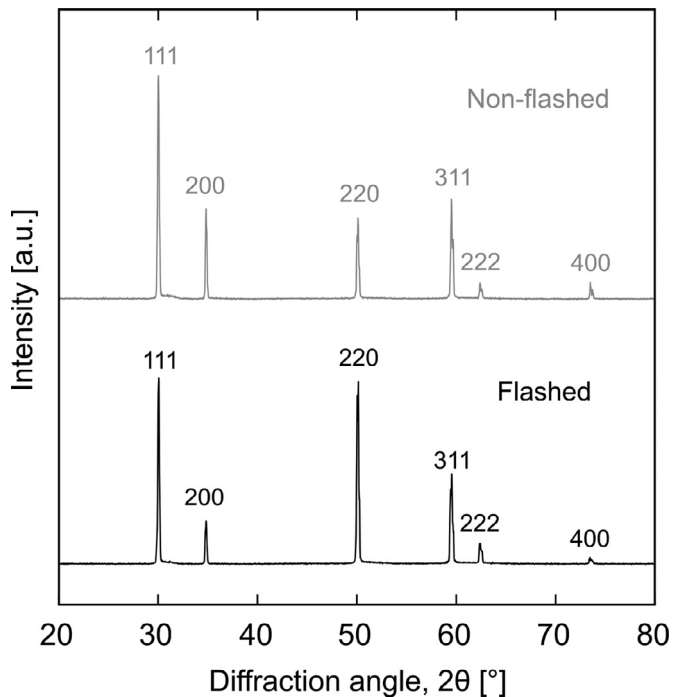
Fig. 7 compares the nanoindentation creep behaviors at 5 mN for 200 s. The flashed sample exhibits a more significant creep at the peak force relatively to the non-flashed one. Such a time-dependent behavior is also confirmed in the loading segment as the softening trend of the flashed sample (Fig. 7a). The difference in creep rates (i.e., the slopes of Fig. 7b) is the most distinctive in the initial 20 s, where the displacement increase was significantly faster in the flashed one. In contrast, the creep rates after 20 s are almost comparable in both samples. The latter range could be dominated by time-dependent plasticity, which was negligibly affected by the flash processing, as also confirmed in the rate-controlled experiments (Fig. 6).

The effective strain rate  $\dot{\epsilon}_{\text{eff}}$  of the flashed sample was 2–3 times higher than the non-flashed one in the initial 5 s, while their significant difference was gradually reduced in 20 s with data uncertainty caused by tip drifts (Fig. 7c). Such a significant creep response of the flashed sample can be attributed to the time-dependent anelastic deformation as well as those observed in the rate-dependent experiments (Figs. 5 and 6).

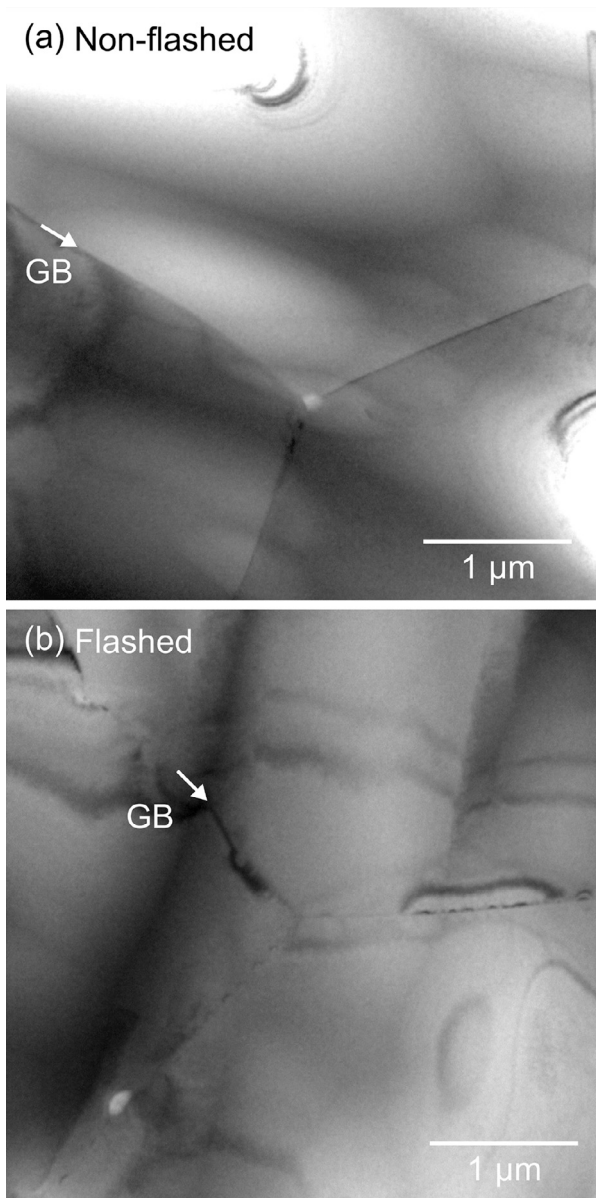
### 3.4. Crystal structures and microstructures

Fig. 8 shows XRD profiles of the flashed and non-flashed samples. Only the fluorite cubic structure was confirmed with no additional peak even after the flash. The variations in relative peak intensities between the two samples are not intrinsic but due to the limited sample dimensions and the coarse grain sizes. These observations suggest that the long-range crystal structural change, such as phase transformation and/or emergence of secondary phases, did not occur during the AC flash processing.

Fig. 9 shows the representative TEM bright-field images. The smooth grain boundaries and low dislocation densities at grain interiors are confirmed in the flashed and non-flashed samples. No particular differences in the microstructures and electron diffractions were recognized from this observation. Although a recent report suggested the contribution of pre-existing dislocations to



**Fig. 8.** XRD profiles of non-flashed (gray) and flashed (black) samples measured in the angular range of  $2\theta = 20^\circ$ – $80^\circ$



**Fig. 9.** Representative TEM bright-field micrographs around grain boundary (GB) triple junctions of (a) non-flashed and (b) flashed samples.

the anelastic behavior of flash-sintered 3YSZ [41], such pre-existing dislocations could not play the predominant role in this study.

Fig. 10 shows inverse pole figure (IPF) maps obtained by EBSD measurement. The average grain size was measured as  $d_{avg} = 11.0 \pm 4.7 \mu\text{m}$  and  $d_{avg} = 11.9 \pm 5.6 \mu\text{m}$  for the non-flashed and flashed samples, respectively. This minute grain size evolution suggests that grain boundary migration was less extensive during the flash process. The consistent results were also obtained from SEM study (Supplementary Fig. S4). The intragranular orientations are uniform even after flash with negligible sub-boundary formation and/or crystal rotations. The impression arrays are visible in Fig. 10b and d, indicating that the nanoindentation measurements were mostly performed at grain interiors. Hence, the flash-induced anelasticity detected in this study were attributed to defect nucleation at grain interiors, which was unassociated with the long-range structural change and increasing dislocation density. These result imply that a short-range structural change induced by the flash processing contributed to the anelasticity, as discussed later.

## 4. Discussion

### 4.1. Anelasticity and point defect activities

In this study, dynamic and quasi-static mechanical properties of cubic zirconia were evaluated before and after AC flash processing. Both the dynamic and quasi-static elastic moduli of the non-flashed sample ( $E$  and  $E^*$ ) were at the standard levels of 8YSZ polycrystals, as summarized in Table 2 [51–57], indicating that the non-flashed sample was almost elastoplastic. The dynamic elastic properties demonstrated a negligible change even after flash (Fig. 2 and Table 1); true elastic softening (i.e., change in the elastic constants) was not confirmed in this study. In contrast, the quasi-static contact modulus considerably decreased with the significant rate dependence after flash (Fig. 5a). This trend is possibly attributed to the rate-dependent and recoverable anelastic deformation, which was also reflected in the impression analysis (Figs. 4 and 6). The flashed sample also showed a faster nanoindentation creep in the initial 20 s rather than the non-flashed one (Fig. 7). Similar rate dependence and reduction in the  $E^*$  and  $H$  values were also recognized in AC-flashed 3YSZ (Supplementary Figs. S2 and S3). This anelasticity (i.e., viscoelasticity or pseudoelasticity in other terms) of the flashed sample was unaffected by the pre-existing dislocations (Fig. 9), but possibly due to the stress-induced and thermally activated recoverable motions of point defects [58,59].

Anelasticity in fluorite-structured oxides (e.g., YSZ and doped ceria) has been studied conventionally by internal friction measurements [56,59,60] and room-temperature creep experiments [61–65]. In YSZ, the internal friction at middle temperatures (ca. 300°C–700°C) excessively decreases the quasi-static elastic modulus from the thermal expansion model [56]. Furthermore, creep strains accumulate even at room temperature during flexural deformation of YSZ [61–63] and nanoindentation of doped ceria [64,65]. This literature has attributed such anelastic behaviors to stress-induced reorientation of dopant cation (e.g.,  $\text{Y}^{3+}$  in YSZ) and neighboring oxygen vacancy pairs, which behave as elastic dipoles responsible for external stress [59–63]. This mechanism is also similar to that of defect-induced ferroics [66,67]. Such anelasticity is a thermally activated process, affecting quasi-static mechanical properties with rate and time dependence rather than dynamic ones. Furthermore, the latest report on flash-induced elastic softening of 3YSZ in the *in-situ* resonance measurement [27] might catch a similar anelastic effect. In this literature, the resonance frequencies of 70–80 Hz at 1000°C–1400°C could be at a quasi-static level, where anelasticity (and resultant internal friction) might contribute to the apparent decrease in Young's modulus.

Despite the above similarities of the present findings to the known anelasticity, we should still be careful to discuss this as an extension of conventional understanding. According to the literature [61–63], even the non-flashed YSZ exhibits anelastic creep at room temperature. However, in this study, the anelastic creep strain was observed only in the flashed sample (Fig. 7c). The non-flashed one might also possess anelasticity, whereas it was less dominant than the time-dependent plasticity that was possibly mediated by dislocation activities [51]. Furthermore, anelasticity in the flashed sample resulted in the apparent decrease in quasi-static elastic modulus even at room temperature (Fig. 5a). This effect was not observed in the non-flashed sample but was expected only above middle temperatures of 300°C–700°C [56,59,60]. Interestingly, the flash-induced decrease in Young's modulus (possibly due to the anelastic effect) [27] was confirmed at considerably higher temperatures (ca. 1000°C–1400°C), where the conventional anelasticity should be less dominant. These results suggest that flash-induced anelasticity is active in a broader temperature range than conventional one.

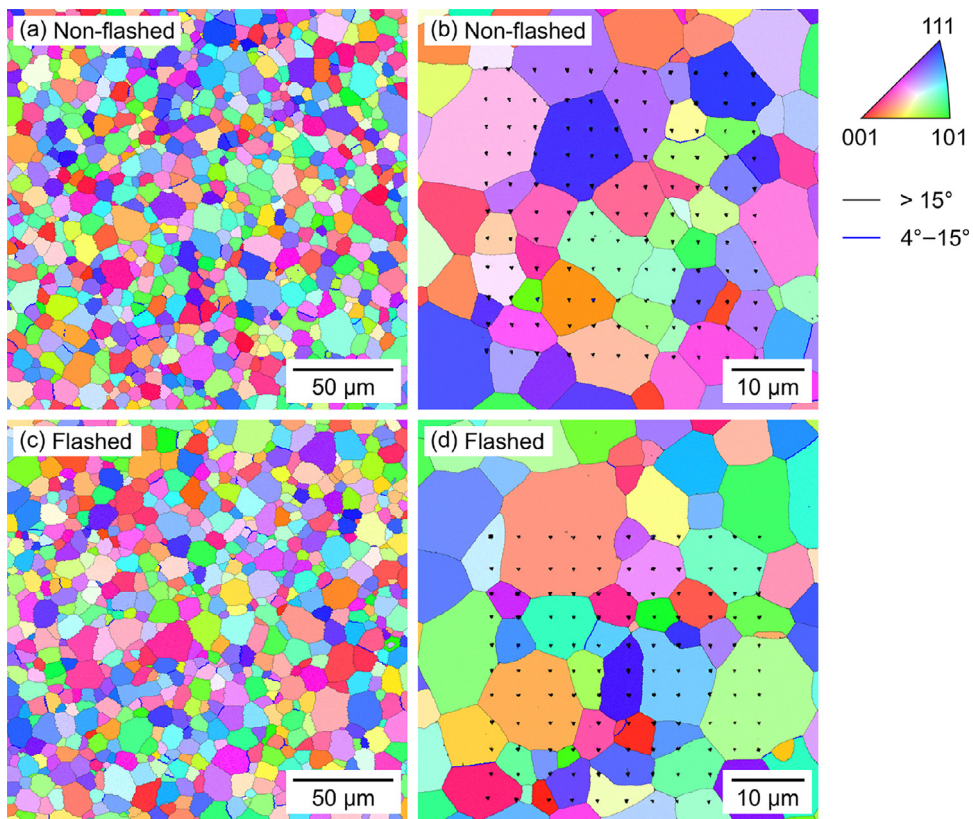


**Fig. 10.** IPF maps of (a) (b) non-flashed and (c) (d) flashed samples obtained by EBSD measurements. Image quality maps were superimposed on the high-resolution images (b, d) to visualize the nanoindentation arrays (black dots). The applied field direction was horizontal.

**Table 2**

Literature data on the contact moduli,  $E^*$ , measured by nanoindentation and theoretical contact moduli,  $E_{th}^*$ , calculated from the reported dynamic Young's moduli,  $E$ , and Poisson's ratios,  $\nu$ , of 8YSZ polycrystals [51–57].

Method	$E^*/\text{GPa}$	$E_{th}^*/\text{GPa}$	$E/\text{GPa}$	$\nu$	Refs.
Nanoindentation	225				Masuda et al. [51]
	218–228				Lian et al. [52]
	197–223				Morales et al. [53]
	217				Wang et al. [54]
	220				This study (non-flashed)
Impulse excitation		189	205	0.31	Giraud and Caneil [55]
Resonance		182	193	0.33	Kimura et al. [56]
Sound velocity measurement		196	216	0.30	Henry et al. [57]
		211	231	0.327	This study (non-flashed)

The differences between the conventional and present anelasticity may be due to the different point defects contributing to these behaviors. Not only the dopant cation and oxygen vacancy dipoles but any point defect forming an anisotropic stress field, including Frenkel pairs and interstitial ions, may contribute to this anelasticity. However, the local structure of such point defects was not revealed in the XRD spectrum (Fig. 8), which could be rather associated with short-range structural change.

#### 4.2. Insights into flash events

The anelastic point defects could be introduced by the thermoelectric effects during AC flash processing. The spatial distributions of  $E^*$  and  $H$  may reflect the local intensities of the field strengths, current densities, temperatures, and their time histories during flash (Fig. 3). The formation of these point defects might not be due to a long-range electrochemical reaction observed after DC flash sintering [10,33–35] but rather a short-range structural change that is possible even in the AC flash.

This anelastic effect was detected by the *ex-situ* quasi-static mechanical characterization after the flash and quench. The effectiveness of quench was recently highlighted by Grimely et al. [17]. They demonstrated an increase in the grain boundary conductivity of 8YSZ after the AC flash and quench with an effective cooling rate of approximately  $15^\circ\text{C}\cdot\text{s}^{-1}$ . In contrast, the maximum quench rate in this study exceeded  $300^\circ\text{C}\cdot\text{s}^{-1}$  (Fig. 1f) and could partially freeze the flash-induced anelastic defects at grain interiors. It should be noted that moderate recovery of oxygen-related defects might occur during the furnace cooling since oxygen ionic diffusion cannot be ignored even at  $600^\circ\text{C}$ . Nevertheless, *in-situ* nanoindentation under a flash state is technically difficult; therefore, *ex-situ* study after flash and quench is currently one of the best solutions to evaluate anelasticity.

The rationalization of the flash-induced point defect structures and the mechanism of their contribution to the athermal effect on ionic-diffusion kinetics is expected in future work. In our preliminary study, the photoluminescence (PL) and Raman spectra of the flashed and non-flashed samples were investigated (Supple-

mentary Figs. S5 and S6). The right shoulder of the PL excitation peak around 275 nm and corresponding weak PL emission around 450 nm are significantly observed in the flashed sample. It was reported that the PL emission near 450 nm in zirconia is associated with oxygen vacancies as the luminescent center [40,68]. However, a negligible difference in the Raman spectra was recognized between the flashed and non-flashed samples. These results imply the contribution of oxygen-related but Raman-inactive defects in the anelastic behavior.

It will be important to determine whether the anelastic point defects enhance ionic diffusion. In this viewpoint, the dopant cation and oxygen vacancy dipoles may be disadvantageous since this dipolar defect leads to a structural ordering which retards ionic mobility [69,70]. Interestingly, in doped ceria, anelasticity (viscoelasticity termed in the literature) was observed via a nanoindentation technique only in disordered structures with low dopant concentrations [71]. Furthermore, it is also important to determine whether the defect and its contribution to the enhanced diffusion can be applied to non-doped but flash-sinterable ceramics.

## 5. Conclusions

This study characterized the physical properties of the flash-induced point defects which may contribute to the athermal effect of electric fields and/or currents on the enhanced ionic diffusion during flash sintering. Conventionally sintered 8YSZ with a fluorite cubic structure was flashed and quenched using an AC electric field and characterized in the viewpoints from dynamic and quasi-static mechanical properties, crystal structures, and microstructures. The following conclusions are drawn:

- (1) The flash-induced point defect structures, along with a negligible effect of long-range electrochemical reactions, could be partially frozen using an AC flash and quench process with its maximum cooling rate exceeding  $300^{\circ}\text{C}\cdot\text{s}^{-1}$  down to the furnace temperature of  $600^{\circ}\text{C}$  which is near the lower bound for oxygen diffusion in YSZ.
- (2) Dynamic elastic properties obtained via sound velocity measurements showed negligible differences between flashed and non-flashed samples. True elastic softening (i.e., change in the elastic constants) was not observed in this study.
- (3) Quasi-static contact modulus of the flashed sample characterized by nanoindentation measurements considerably decreased with a substantial rate dependence (i.e., the slower the loading rate, the lower the measured contact modulus), while the non-flashed one was almost rate-independent. The contact modulus of the flashed sample tested at the slowest loading rate of  $1 \times 10^{-1} \text{ mN}\cdot\text{s}^{-1}$  was approximately 72% of the non-flashed one.
- (4) The above rate-dependent behaviors were characterized as anelasticity attributed to stress-induced recoverable motions of point defects, with a negligible effect of pre-existing dislocations. The anelasticity observed in this study was possibly caused by defect nucleation at grain interiors during flash, as evidenced by lack of grain boundary migration in the process. The anelastic point defects might be associated with short-range structural change possible even in the AC flash, as suggested by the negligible change in the microstructure and long-range crystal structure.

## Declaration of Competing Interest

The authors declare that they have no known competing financial interests or personal relationships that could have appeared to influence the work reported in this paper.

## Acknowledgments

This study was financially supported by JST CREST "Nanomechanics" (JPMJCR1996) and JSPS KAKENHI "Grant-in-Aid for Early-Career Scientists" (20K15018) and "Grant-in-Aid for Scientific Research on Innovative Areas" (19H05792). A part of this work was performed by "Nanotechnology Platform Project" operated by the Ministry of Education, Culture, Sports, Science and Technology (MEXT), Japan, at the University of Tokyo (JPMXP09-A-21-UT-0002) and National Institute for Materials Science (JPMXP09-S-20-NM-0058). The authors appreciate Enago ([www.enago.jp](http://www.enago.jp)) for the English proofreading.

## Supplementary materials

Supplementary material associated with this article can be found, in the online version, at [doi:10.1016/j.actamat.2022.117704](https://doi.org/10.1016/j.actamat.2022.117704).

## References

- [1] M. Cologna, B. Rashkova, R. Raj, Flash sintering of nanograin zirconia in  $< 5\text{s}$  at  $850^{\circ}\text{C}$ , *J. Am. Ceram. Soc.* 93 (2010) 3556–3559.
- [2] M. Cologna, A.L.G. Prette, R. Raj, Flash-sintering of cubic yttria-stabilized zirconia at  $750^{\circ}\text{C}$  for possible use in SOFC manufacturing, *J. Am. Ceram. Soc.* 94 (2011) 316–319.
- [3] M. Cologna, J.S.C. Francis, R. Raj, Field assisted and flash sintering of alumina and its relationship to conductivity and MgO-doping, *J. Eur. Ceram. Soc.* 31 (2011) 2827–2837.
- [4] A.L.G. Prette, M. Cologna, V. Sgavio, R. Raj, Flash-sintering of  $\text{Co}_2\text{MnO}_4$  spinel for solid oxide fuel cell applications, *J. Power Sources* 196 (2011) 2061–2065.
- [5] A. Karakuscu, M. Cologna, D. Yarotski, J. Won, J.S.C. Francis, R. Raj, B.P. Uberuaga, Defect structure of flash-sintered strontium titanate, *J. Am. Ceram. Soc.* 95 (2012) 2531–2536.
- [6] H. Yoshida, Y. Sakka, T. Yamamoto, J.M. Lebrun, R. Raj, Densification behaviour and microstructural development in undoped yttria prepared by flash-sintering, *J. Eur. Ceram. Soc.* 34 (2014) 991–1000.
- [7] J.C. M'Peko, J.S.C. Francis, R. Raj, Field-assisted sintering of undoped  $\text{BaTiO}_3$ : microstructure evolution and dielectric permittivity, *J. Eur. Ceram. Soc.* 34 (2014) 3655–3660.
- [8] H. Yoshida, P. Biswas, R. Johnson, M.K. Mohan, Flash-sintering of magnesium aluminate spinel ( $\text{MgAl}_2\text{O}_4$ ) ceramics, *J. Am. Ceram. Soc.* 100 (2017) 554–562.
- [9] D. Yadav, R. Raj, Two unique measurements related to flash experiments with yttria-stabilized zirconia, *J. Am. Ceram. Soc.* 100 (2017) 5374–5378.
- [10] M. Biesuz, L. Pinter, T. Saunders, M. Reece, J. Binner, V.M. Sgavio, S. Grasso, Investigation of electrochemical, optical and thermal effects during flash sintering of 8YSZ, *Materials* 11 (2018) 1214 (Basel).
- [11] H. Yoshida, Y. Sasaki, Low temperature and high strain rate superplastic flow in structural ceramics induced by strong electric field, *Scr. Mater.* 146 (2018) 173–177.
- [12] Y. Sasaki, K. Morita, T. Yamamoto, K. Soga, H. Masuda, H. Yoshida, Electric current dependence of plastic flow behavior with large tensile elongation in tetragonal zirconia polycrystal under a DC field, *Scr. Mater.* 194 (2021) 113659.
- [13] K. Morita, F. Naito, D. Terada, Microcrack healing in zirconia ceramics under a DC electric field/current, *J. Eur. Ceram. Soc.* 41 (2021) 282–289.
- [14] R.I. Todd, E. Zapata-Solvas, R.S. Bonilla, T. Sneddon, P.R. Wilshaw, Electrical characteristics of flash sintering: thermal runaway of Joule heating, *J. Eur. Ceram. Soc.* 35 (2015) 1865–1877.
- [15] W. Rheinheimer, X.L. Phuah, H. Wang, F. Lemke, M.J. Hoffmann, H. Wang, The role of point defects and defect gradients in flash sintering of perovskite oxides, *Acta Mater.* 165 (2019) 398–408.
- [16] H. Charalambous, S.K. Jha, J. Okasinski, T. Tsakalakos, Spectral analysis and temperature measurement during flash sintering under AC electric field, *Materialia* 6 (2019) 100273.
- [17] C.A. Grimley, S. Funni, C. Green, E.C. Dickey, A thermal perspective of flash sintering: the effect of AC current ramp rate on microstructure evolution, *J. Eur. Ceram. Soc.* 41 (2021) 2807–2817.
- [18] K. Nambu, K. Morita, K. Soga, T. Yamamoto, H. Masuda, H. Yoshida, Densification of  $\text{Y}_2\text{O}_3$  by flash sintering under an AC electric field, *J. Eur. Ceram. Soc.* 42 (2022) 567–575.
- [19] R. Raj, Joule heating during flash-sintering, *J. Eur. Ceram. Soc.* 32 (2012) 2293–2301.
- [20] M. Biesuz, V.M. Sgavio, Flash sintering of ceramics, *J. Eur. Ceram. Soc.* 39 (2019) 115–143.
- [21] R. Raj, A. Kulkarni, J.M. Lebrun, S. Jha, Flash sintering: a new frontier in defect physics and materials science, *MRS Bull.* 46 (2021) 36–43.
- [22] O. Guillon, R.A. De Souza, T.P. Mishra, W. Rheinheimer, Electric-field-assisted processing of ceramics: nonthermal effects and related mechanisms, *MRS Bull.* 46 (2021) 52–58.
- [23] R. Raj, M. Cologna, J.S.C. Francis, Influence of externally imposed and internally generated electrical fields on grain growth, diffusional creep, sintering and related phenomena in ceramics, *J. Am. Ceram. Soc.* 94 (2011) 1941–1965.

- [24] J.M. Lebrun, C.S. Hellberg, S.K. Jha, W.M. Kriven, A. Steveson, K.C. Seymour, N. Bernstein, S.C. Erwin, R. Raj, *In-situ* measurements of lattice expansion related to defect generation during flash sintering, *J. Am. Ceram. Soc.* 100 (2017) 4965–4970.
- [25] B. Yoon, D. Yadav, R. Raj, E. Sortino, S. Ghose, P. Sarin, D. Shoemaker, Measurement of O and Ti atom displacements in  $TiO_2$  during flash sintering experiments, *J. Am. Ceram. Soc.* 101 (2018) 1811–1817.
- [26] T.P. Mishra, R.R.I. Neto, R. Raj, O. Guillon, M. Bram, Current-rate flash sintering of gadolinium doped ceria: microstructure and defect generation, *Acta Mater.* 189 (2020) 145–153.
- [27] R. Kathiria, D.E. Wolf, R. Raj, M. Jongmanns, Frenkel pairs cause elastic softening in zirconia: theory and experiments, *New J. Phys.* 23 (2021) 053013.
- [28] M. Jongmanns, R. Raj, D.E. Wolf, Generation of Frenkel defects above the Debye temperature by proliferation of phonons near the Brillouin zone edge, *New J. Phys.* 20 (2018) 093013.
- [29] M. Jongmanns, D.E. Wolf, Element-specific displacements in defect-enriched  $TiO_2$ : indication of a flash sintering mechanism, *J. Am. Ceram. Soc.* 103 (2020) 589–596.
- [30] W. Xu, A. Maksymenko, S. Hasan, J.J. Meléndez, E. Olevsky, Effect of external electric field on diffusivity and flash sintering of 8YSZ: a molecular dynamics study, *Acta Mater.* 206 (2021) 116596.
- [31] M. Schie, S. Menzel, J. Robertson, R. Waser, R.A. De Souza, Field-enhanced route to generating anti-Frenkel pairs in  $HfO_2$ , *Phys. Rev. Mater.* 2 (2018) 035002.
- [32] K. Ren, S. Huang, Y. Cao, G. Shao, Y. Wang, The densification behavior of flash sintered  $BaTiO_3$ , *Scr. Mater.* 186 (2020) 362–365.
- [33] H. Yoshida, K. Morita, B.N. Kim, Y. Sakka, T. Yamamoto, Reduction in sintering temperature for flash-sintering of yttria by nickel cation-doping, *Acta Mater.* 106 (2016) 344–352.
- [34] H. Charalambous, S.K. Jha, H. Wang, X.L. Phuah, H. Wang, T. Tsakalakos, Inhomogeneous reduction and its relation to grain growth of titania during flash sintering, *Scr. Mater.* 155 (2018) 37–40.
- [35] T.P. Mishra, R.R.I. Neto, G. Speranza, A. Quaranta, V.M. Sglavo, R. Raj, O. Guillon, M. Bram, M. Biesuz, Electronic conductivity in gadolinium doped ceria under direct current as a trigger for flash sintering, *Scr. Mater.* 179 (2020) 55–60.
- [36] J.M. Lebrun, T.G. Morrissey, J.S.C. Francis, K.C. Seymour, W.M. Kriven, R. Raj, Emergence and extinction of a new phase during on-off experiments related to flash sintering of 3YSZ, *J. Am. Ceram. Soc.* 98 (2015) 1493–1497.
- [37] H. Charalambous, S.K. Jha, J.S. Okasinski, T. Tsakalakos, Generation of electric-field stabilized zirconium monoxide secondary phase within cubic zirconia, *Scr. Mater.* 190 (2021) 22–26.
- [38] C. Schmerbauch, J. Gonzalez-Julian, R. Röder, C. Ronning, O. Guillon, Flash sintering of nanocrystalline zinc oxide and its influence on microstructure and defect formation, *J. Am. Ceram. Soc.* 97 (2014) 1728–1735.
- [39] K. Nambu, H. Hayasaka, T. Yamamoto, H. Yoshida, Photoluminescence properties of undoped and  $Si^{4+}$ -doped polycrystalline  $Y_2O_3$  phosphors prepared by flash-sintering, *Appl. Phys. Express* 12 (2019) 075504.
- [40] Y. Yamashita, T. Kurachi, T. Tokunaga, H. Yoshida, T. Yamamoto, Blue photo luminescence from 3 mol%  $Y_2O_3$ -doped  $ZrO_2$  polycrystals sintered by flash sintering under an alternating current electric field, *J. Eur. Ceram. Soc.* 40 (2020) 2072–2076.
- [41] J. Cho, Q. Li, H. Wang, Z. Fan, J. Li, S. Xue, K.S.N. Vikrant, H. Wang, T.B. Holland, A.K. Mukherjee, R.E. García, X. Zhang, High temperature deformability of ductile flash-sintered ceramics via *in-situ* compression, *Nat. Commun.* 9 (2018) 2063.
- [42] J. Li, J. Cho, J. Ding, H. Charalambous, S. Xue, H. Wang, X.L. Phuah, J. Jian, X. Wang, C. Ophus, T. Tsakalakos, R.E. García, A.K. Mukherjee, N. Bernstein, C.S. Hellberg, H. Wang, X. Zhang, Nanoscale stacking fault-assisted room temperature plasticity in flash-sintered  $TiO_2$ , *Sci. Adv.* 5 (2019) eaaw5119.
- [43] J. Cho, X.L. Phuah, J. Li, Z. Shang, H. Wang, H. Charalambous, T. Tsakalakos, A.K. Mukherjee, H. Wang, X. Zhang, Temperature effect on mechanical response of flash-sintered ZnO by *in-situ* compression tests, *Acta Mater.* 200 (2020) 699–709.
- [44] Y. Yoshizawa, T. Sakuma, Evolution of microstructure and grain growth in  $ZrO_2-Y_2O_3$  alloys, *ISIJ Int.* 29 (1989) 746–752.
- [45] M.F. Hoedl, E. Makagon, I. Lubomirsky, R. Merkle, E.A. Kotomin, J. Maier, Impact of point defects on the elastic properties of  $BaZrO_3$ : comprehensive insight from experiments and ab initio calculations, *Acta Mater.* 160 (2018) 247–256.
- [46] W.C. Oliver, G.M. Pharr, An improved technique for determining hardness and elastic modulus using load and displacement sensing indentation experiments, *J. Mater. Res.* 7 (1992) 1564–1583.
- [47] F. Szuecs, M. Werner, R.S. Sussmann, C.S.J. Pickles, H.J. Fecht, Temperature dependence of young's modulus and degradation of chemical vapor deposited diamond, *J. Appl. Phys.* 86 (1999) 6010–6017.
- [48] W.H. Poisl, W.C. Oliver, B.D. Fabes, The relationship between indentation and uniaxial creep in amorphous selenium, *J. Mater. Res.* 10 (1995) 2024–2032.
- [49] H.M. Kandil, J.D. Greiner, J.F. Smith, Single-crystal elastic constants of yttria-stabilized zirconia in the range 20° to 700°C, *J. Am. Ceram. Soc.* 67 (1984) 341–346.
- [50] R.L. Fullman, Measurement of particle sizes in opaque bodies, *JOM* 5 (1953) 447–452.
- [51] H. Masuda, K. Morita, T. Ohmura, Nanoindentation-induced plasticity in cubic zirconia up to 500°C, *Acta Mater.* 184 (2020) 59–68.
- [52] J. Lian, J.E. Garay, J. Wang, Grain size and grain boundary effects on the mechanical behavior of fully stabilized zirconia investigated by nanoindentation, *Scr. Mater.* 56 (2007) 1095–1098.
- [53] M. Morales, J.J. Roa, X.G. Capdevila, M. Segarra, S. Piñol, Mechanical properties at the nanometer scale of GDC and YSZ used as electrolytes for solid oxide fuel cells, *Acta Mater.* 58 (2010) 2504–2509.
- [54] Y. Wang, K. Duncan, E.D. Wachsmann, F. Ebrahimi, The effect of oxygen vacancy concentration on the elastic modulus of fluorite-structured oxides, *Solid State Ion.* 178 (2007) 53–58.
- [55] S. Giraud, J. Caneil, Young's modulus of some SOFCs materials as a function of temperature, *J. Eur. Ceram. Soc.* 28 (2008) 77–83.
- [56] Y. Kimura, T. Kushi, A. Unemoto, K. Amezawa, T. Kawada, Influence of aging on mechanical properties of yttria-doped zirconia, *Ceramics* 1 (2018) 287–303.
- [57] R. Henry, T. Blay, T. Douillard, A. Descamps-Mandine, I. Zacharie-Aubrun, J.M. Gatt, C. Langlois, S. Meille, Local fracture toughness measurements in polycrystalline cubic zirconia using micro-cantilever bending tests, *Mech. Mater.* 136 (2019) 103086.
- [58] G. Cheng, C. Miao, Q. Qin, J. Li, F. Xu, H. Haftbaradaran, E.C. Dickey, H. Gao, Y. Zhu, Large anelasticity and associated energy dissipation in single-crystalline nanowires, *Nat. Nanotechnol.* 10 (2015) 687–692.
- [59] M. Weller, Anelastic relaxation of point defects in cubic crystals, *J. Phys.* 06 (1996) C8–63 IV FranceC8–72.
- [60] M. Weller, A. Lakki, Defects in cubic zirconia studied by mechanical loss spectroscopy, *Ber. Bunsenges. Phys. Chem.* 101 (1997) 1297–1302.
- [61] M. Matsuzawa, S. Horibe, Analysis of non-elastic strain produced in zirconia ceramics, *Mater. Sci. Eng. A* 346 (2003) 75–82.
- [62] M. Matsuzawa, M. Abe, S. Horibe, J. Sakai, The effect of reduction on the mechanical properties of  $CeO_2$  doped tetragonal zirconia ceramics, *Acta Mater.* 52 (2004) 1675–1682.
- [63] Y. Okada, M. Matsuzawa, S. Horibe, Crystal orientation dependence of anelastic relaxation in 8Y-fully stabilized zirconia, *J. Mater. Sci.* 42 (2007) 5551–5555.
- [64] R. Korobko, C.T. Chen, S. Kim, S.R. Cohen, E. Wachtel, N. Yavo, I. Lubomirsky, Influence of Gd content on the room temperature mechanical properties of Gd-doped ceria, *Scr. Mater.* 66 (2012) 155–158.
- [65] E. Wachtel, A.I. Frenkel, I. Lubomirsky, Anelastic and electromechanical properties of doped and reduced ceria, *Adv. Mater.* 30 (2018) 1707455.
- [66] R.K. Singhal, S. Kumar, P. Kumar, Y.T. Xing, E. Saitovitch, Evidence of defect-induced ferromagnetism and its "switch" action in pristine bulk  $TiO_2$ , *Appl. Phys. Lett.* 98 (2011) 092510.
- [67] O. Aktas, S. Crossley, M.A. Carpenter, E.K.H. Salje, Polar correlations and defect-induced ferroelectricity in cryogenic  $KTaO_3$ , *Phys. Rev. B* 90 (2014) 165309.
- [68] K. Iwasaki, Y. Takahashi, N. Terakado, N. Onoue, T. Shinozaki, T. Fujiwara, Prominent long-lasting photoluminescence in defect-activated zirconia: a rare-earth free and accessible phosphor, *Ceram. Int.* 44 (2018) 12929–12933.
- [69] K. Kawata, H. Maekawa, T. Nemoto, T. Yamamura, Local structure analysis of YSZ by  $Y-8Y$  MAS-NMR, *Solid State Ion.* 177 (2006) 1687–1690.
- [70] M. Ozawa, K. Imura, Oxygen relaxation and oxide ion conduction of  $Zr_{0.8-x}Ce_xY_{0.2}O_{1.9}$  ( $x = 0, 0.3, 0.5$ ), *Solid State Ion.* 262 (2014) 526–529.
- [71] M. Varenik, S. Cohen, E. Wachtel, A.I. Frenkel, J.C. Nino, I. Lubomirsky, Oxygen vacancy ordering and viscoelastic mechanical properties of doped ceria ceramics, *Scr. Mater.* 163 (2019) 19–23.